Journal of Materials Chemistry A

ROYAL SOCIETY OF CHEMISTRY

PAPER

View Article Online
View Journal

Cite this: DOI: 10.1039/d6ta01141a

Biomass-derived potassium-doped reduced graphene oxide-like material for high-performance supercapacitors: experimental and computational analysis

Chetna Tewari,[a] Kundan Singh Rawat,[a] Diksha Bhatt,[b] Boddepalli SanthiBhushan,[c] Young Nam Kim,[a] Somi Yoon,[ad] Anurag Srivastava,[e] Jun-Wei Zha,[f] Nanda Gopal Sahoo[b] and Yong Chae Jung *[a]

With the growing energy demand and limited resources, the development of cost-effective and efficient materials is essential. Among these, carbon-based nanomaterials offer promising characteristics for energy applications. Bio-based carbon nanomaterials are particularly promising for energy storage devices like supercapacitors due to their sustainability and performance characteristics. This study presents a cost-effective method for synthesizing a bio-based reduced graphene oxide (rGO)-like material using persimmon fruit, a readily available resource in East Asia. A clean two-step thermal process was employed to synthesize an rGO-like material, eliminating the need for toxic chemicals commonly used in conventional approaches. The material is derived from persimmon and naturally doped with potassium, which contributes to enhanced supercapacitor performance. A systematic optimization of carbonization temperature (600–1000 °C) and heating rate (5–15 °C min^{-1}) was carried out using residual yield analysis, Raman spectroscopy, XRD, and TGA, identifying 800 °C and 10 °C min^{-1} as the optimal synthesis conditions. Density Functional Theory (DFT) calculations were performed to elucidate the electronic structure and validate the improved electrochemical properties observed experimentally. The electrochemical performance of the synthesized material was investigated in acidic, basic, and neutral electrolytes, using a three-electrode setup. The maximum C_s achieved was 302 F g^{-1} at a scan rate of 2 mV s^{-1} in an acidic electrolyte. Furthermore, a symmetric supercapacitor device fabricated using the synthesized material demonstrated a specific capacitance of 98 F g^{-1}, an energy density of 11 Wh kg^{-1}, and a power density of 89.8 W kg^{-1} at a current density of 0.2 A g^{-1}. Remarkably, the device maintained its original capacitance even after 5000 charge–discharge cycles. These results highlight the potential of potassium-doped, biomass-derived rGO-like materials as effective electrode materials for supercapacitor applications.

Received 6th February 2026
Accepted 19th May 2026

DOI: 10.1039/d6ta01141a

rsc.li/materials-a

1. Introduction

Research into energy storage devices has gained significant momentum due to the increasing demand for high-performance electronics and renewable energy sources.[1,2] Supercapacitors (SCs) have emerged as promising candidates for energy storage due to their extended cycle life, high power density, and rapid charge–discharge rates.[3,4] The performance of SCs is heavily influenced by electrode materials, with carbon-based nanomaterials such as zero-dimensional carbon spheres, one-dimensional carbon nanotubes, two-dimensional graphene, and three-dimensional hydrogels/aerogels being extensively studied.[5–7] Among these, graphene stands out due to its exceptional properties including high surface area, porosity, two-dimensional structure, and excellent electrical conductivity.[8]

[a]RAMP Convergence Research Center, Korea Institute of Science and Technology (KIST), 92 Chudong-ro, Bongdong-eup, Wanju-gun, Jeonbuk, 55324, Republic of Korea. E-mail: ycjung@kist.re.kr

[b]Prof. Rajendra Singh Nanoscience and Nanotechnology Centre, Department of Chemistry D.S.B. Campus, Kumaun University Nainital, Uttarakhand, India

[c]Department of Electronics and Communications Engineering, Indian Institute of Information Technology, Allahabad, UP-211015, India

[d]Department of Organic and Nano Engineering, Hanyang University, 222 Wangsimni-ro, Seongdong-gu, Seoul 04763, Republic of Korea

[e]Department of Engineering Sciences, ABV – Indian Institute of Information Technology and Management, Gwalior, M.P. – 474015, India

[f]State Key Laboratory of Alternate Electrical Power System with Renewable Energy Sources, School of Electrical and Electronic Engineering, North China Electric Power University, Beijing 102206, China

Research has shown that introducing metallic and non-metallic elements alters surface properties and enhances conductivity.[9] For instance, Morenghi *et al.* demonstrated a graphene electrode coated with nickel nanoparticles achieving specific energy and power densities of 37 Wh kg^{-1} and 5 kW kg^{-1}, respectively.[10] Heteroatom doping techniques such as solution-based doping, gas-phase doping, and others have been employed to enhance electronic properties and tailor surface chemistry, although natural metal doping remains less explored.

While graphene-based materials exhibit superior electrochemical performance, their high cost, complex manufacturing processes, and environmental impact pose challenges.[6] Recent studies have shifted toward developing scalable and cost-effective synthesis methods for graphene-like materials, with a focus on structural design and electrochemical optimization. Biomass, being rich in carbohydrates, fibers, and minerals, is considered a sustainable and versatile precursor for carbon-based materials.[11,12] Biomass-derived graphene-based materials have garnered attention for their affordability, renewability, and eco-friendliness.[3] For instance, Cao *et al.* developed lignin-based aerogels with organized structures, achieving an energy density of 32 Wh kg^{-1},[13] and Wang *et al.* synthesized cellulose nanofiber/multi-walled carbon nanotube composites with a specific capacitance of 114.8 F g^{-1}.[14] Akhavan *et al.* used a modified Hummers method to synthesize reduced graphene oxide (rGO) from various industrial carbonaceous wastes, including fruit and agricultural residues.[15] Similarly, large-scale production of graphene-based materials has been reported from waste tires,[16] plastics,[17–19] and agricultural biomass[20–22] for supercapacitor applications. However, reports on the synthesis of graphene-like materials from biomass naturally doped with functional metallic elements are still limited.

In particular, potassium doping has emerged as a promising strategy for enhancing the electrochemical performance of supercapacitor electrodes. Potassium incorporation is known to increase electrical conductivity and facilitate fast ion intercalation/deintercalation, resulting in improved specific capacitance and rate capability. For example, potassium-doped Sr–Cu metal oxide ($K–SrCu_2O_2$) showed a much higher capacitance of 438 F g^{-1} at 1 A g^{-1}, compared to just 14.5 F g^{-1} for the undoped material, due to its better charge movement and activated tunnel-like structures.[23] Additionally, potassium-assisted biomass carbonization contributes to the formation of highly porous architectures with abundant active sites, further enhancing capacitance.[24] K-doping in electrolytes also improves ionic conductivity and expands the electrochemical window, enabling higher energy and power densities.[25] These findings collectively underscore potassium's multifaceted role in boosting both electrode and electrolyte performance, making it a valuable dopant in supercapacitor design.

In this context, producing rGO-like materials from unconventional, mineral-rich biomass sources such as persimmon fruit is of growing interest. The Hachiya variety of persimmon, heart- or acorn-shaped and native to east Asia, is rich in soluble tannins and essential minerals including potassium, phosphorus, calcium, magnesium, and zinc.[26,27] Prior studies have shown that doping with elements such as magnesium, potassium, and phosphorus significantly improves supercapacitor performance.[24,28,29] To further highlight the electrochemical potential of biomass-derived carbon materials, a comparative analysis of previously reported carbon-based electrodes is presented in Table S1. This comparison demonstrates that the PrGO synthesized in this study—without the use of any chemical activation agents or catalysts—exhibits a competitive specific capacitance relative to other doped and activated materials, highlighting its potential for energy storage applications.

This study focuses on synthesizing rGO-like carbon materials from Hachiya persimmon fruit through a two-step thermal process. The resulting material is naturally doped with potassium, which is the most abundant metal in persimmon compared to other elements.

Persimmon fruit is characterized by a high moisture content (~80.9%) and a tannin content of approximately 3–4%.[27,30,31] Elemental analysis (per 100 g of persimmon fruit) reveals a significantly higher potassium content (203 ± 24.10 mg) compared to other elements, which are present in relatively low concentrations, such as phosphorus (27 ± 2.66 mg), calcium (16 ± 4.33 mg), magnesium (11 ± 1.80 mg), sodium (10 ± 0.80 mg), iron (0.27 ± 0.08 mg), manganese (0.25 ± 0.04 mg), copper (0.11 ± 0.03 mg), and zinc (0.10 ± 0.02 mg).[27] In addition, the total soluble solids, pH, and protein, vitamin C, and soluble tannin contents of cv. Hachiya are reported as 17.10%, 5.40, 600 mg/100 g, 12 mg/100 g, and 3.15 mg/100 g, respectively.[27]

Consistent with this composition, our results indicate that after pyrolysis, potassium remains present in significant amounts, whereas other metallic elements are retained only at negligible levels. Furthermore, the relatively high potassium content (~2.15 at%) suggests its important role in influencing the structural, electrical, and ion-transport properties of the synthesized rGO. The electrochemical performance of the material was first evaluated in a three-electrode setup using acidic, alkaline, and neutral electrolytes, and the optimized electrolyte (1 M H_2SO_4) was used to evaluate the supercapacitor performance in a two-electrode configuration. Additionally, Density Functional Theory (DFT) analysis was conducted to elucidate the electronic structure and confirm the role of potassium in enhancing charge storage behaviour. This work contributes to the development of cost-effective and high-performance electrode materials for next-generation supercapacitors.

2. Materials and methods

2.1. Materials

Persimmon fruit was obtained from a local market of Jeonju, South Korea. ExcelaR provided the H_3PO_4, while Sigma Aldrich supplied the poly-vinylidene fluoride (PVDF) polymer and H_2SO_4. We used every single chemical exactly as it was provided to us. The graphite sheets utilized as the current collector were supplied by the Madras Asbestos business. Every experiment relied on using double-distilled water.

2.2. Synthesis of the persimmon-derived reduced graphene oxide-like material

The persimmon-based nanomaterial has been developed by an easy and cost-effective two-step thermal treatment as presented in Fig. S1. In brief, fresh persimmon fruit was taken and placed inside the zipper and crushed with the help of a roller to collect the pulp (without the outer cover and seeds). Then, the material was centrifuged at 9000 rpm to collect the fibre part. Further, 75 g of the material was weighed and low temperature carbonization was done in a Teflon hydrothermal reactor with 100 mL capacity inside an oven at 180 °C for 24 h. After this, the reactor was left to cool and reach room temperature and then the resultant brown coloured cylindrical sponge with a weight of 65.36 g was collected (some liquid material was also obtained). This first stage low temperature thermal treatment leads to the carbonization or polymerisation of the tannins present in the fruit and facilitates the formation of a brown coloured hydrogel with a spongy texture and porous nature. Subsequently, the hydrogel was freeze-dried overnight at −40 °C under vacuum conditions of 20 Pa. The dry weight of the resulting material was 7.66 g, indicating that approximately 88% of the original mass corresponded to water/moisture content, which is consistent with previously reported data.[27] The obtained brown cylindrical sponge exhibited a height of 5.7 cm and a diameter of 3.5 cm and was characterized by its low density and porous nature.

In the second stage, the freeze-dried hydrogel was subjected to high-temperature thermal treatment in a tubular furnace under a continuous nitrogen atmosphere to induce thermal reduction and structural ordering. To establish optimal synthesis conditions, the carbonization temperature was systematically varied between 600 and 1000 °C, followed by an evaluation of the heating rate in the range of 5–15 °C min^{-1}. Based on the combined analysis of residual yield, Raman spectroscopy, XRD, and TGA, a carbonization temperature of 800 °C and a heating rate of 10 °C min^{-1} were identified as optimal. Under these conditions, the material was thermally treated, held at the target temperature for 60 min, and subsequently cooled to room temperature at a controlled rate of 2 °C min^{-1}. The resulting conductive carbon material was denoted as PrGO (persimmon-derived potassium-doped reduced graphene oxide–like material).

2.3. Schematic illustration of the formation of the persimmon-derived reduced graphene oxide-like material

The synthesis of PrGO was carried out through a two-step thermal process. In the first step, the fruit undergoes hydrothermal carbonization at a relatively low temperature (180 °C). During this process, macromolecules such as tannins, phenolic compounds, and other unsaturated/aromatic species present in persimmon undergo polymerization, molecular rearrangement, and crosslinking reactions.[32] These transformations result in the formation of a hydrogel-like carbon framework enriched with surface functional groups and containing early-stage graphitic domains. The subsequent freeze-drying step promotes dehydration and preserves the porous, swollen morphology of the intermediate structure.

In the second step, the hydrogel is subjected to high-temperature pyrolysis at 800 °C under an inert atmosphere. During this stage, thermal decomposition initiates nucleation and the growth of small, ordered carbon clusters and aromatic domains. These domains further rearrange and undergo repolymerization to form graphene-like structures, accompanied by the elimination of volatile species such as CH_4, CO, and CO_2. Notably, the naturally abundant potassium content in persimmon may serve as both a chemical activator and dopant, promoting carbon etching, interlayer expansion, defect formation, and enhancement of electrical conductivity. The resulting carbon material exhibits a layered architecture resembling that of reduced graphene oxide. A plausible mechanism is illustrated in Scheme 1.

3. Characterization

3.1. Structural and surface characterization

X-ray diffraction (XRD) patterns were recorded using a Rigaku SmartLab diffractometer (9 kW) with a Cu Kα radiation source ($\lambda = 1.54$ Å) to determine the crystalline or amorphous nature of the samples. Surface morphologies were examined using a Nova NanoSEM 450 scanning electron microscope. Transmission electron microscopy (TEM) was performed with a JEOL-2100 to investigate the internal structure and layered morphology of the persimmon-derived sample. Thermogravimetric analysis (TGA) was carried out to evaluate thermal stability, and Raman spectra were obtained using a Renishaw InVia Raman microscope equipped with a 514 nm laser to analyze the defect structure in the synthesized PrGO. X-ray photoelectron spectroscopy (XPS) was carried out using a K-Alpha spectrometer (Thermo Fisher Scientific, USA) to analyze surface functional groups and elemental composition. As a surface-sensitive, photoelectric effect-based technique, XPS provides quantitative information about the elemental composition and chemical states present on the sample surface.

3.2. Electrode preparation and electrochemical analysis

The material's electrochemical behavior was investigated in three (with 1 M H_2SO_4, 6 M KOH, and 2 M KCl) and two-electrode configurations (with H_2SO_4) in a Metrohm Auto lab electrochemical workstation. PrGO was used as the working electrode, Pt wire as the counter electrode, and Ag/AgCl as the reference electrode in a three-electrode setup. The working electrode was made by coating a graphite sheet (1×1 cm^2) with a combination of 90% PrGO and 10% polyvinylidene fluoride (PVDF). For this, PrGO was dissolved in NMP solvent, and then using a mortar and pestle PVDF was gradually added to generate this homogeneous slurry. Next, this slurry of the produced material was applied to 1×1 cm^2 graphite sheets and dried at 80 °C to create a working electrode. The mass of the active substance in the electrode was around 1 mg. The symmetric supercapacitor device with PrGO as an electrode material was subjected to electrochemical experiments using a two-electrode setup. A symmetric supercapacitor device with PrGO as an electrode material was built using two identical electrodes that

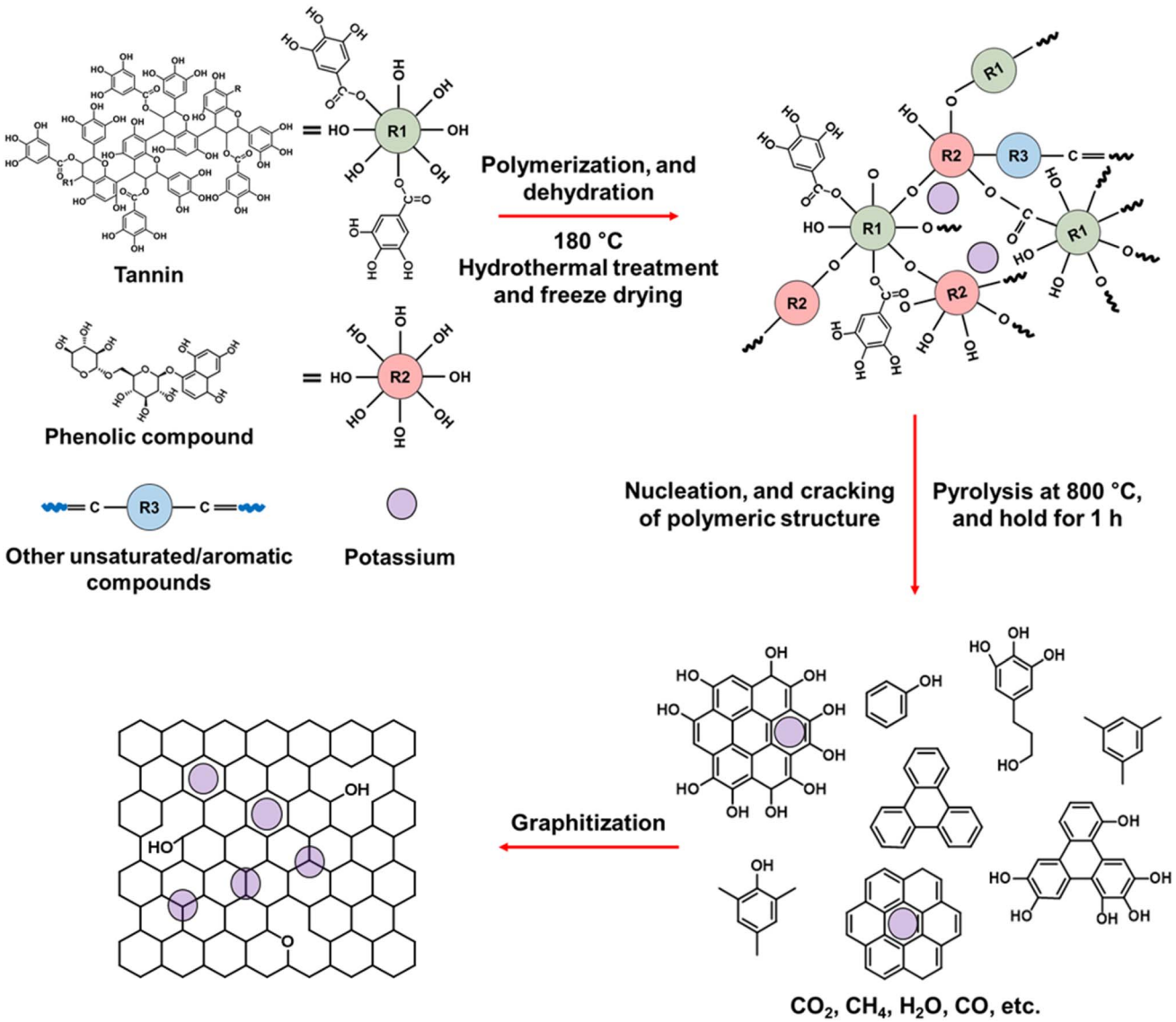

Scheme 1 Illustration of a plausible mechanism for the formation of potassium doped PrGO.

had the same mass (1 mg) of PrGO. Between the electrodes, Whatman filter paper, a porous separator, was used to keep the circuit from shorting while still letting ions pass through. The electrodes were configured in a sandwich arrangement with a 1 M H_2SO_4 aqueous electrolyte, ensuring adequate electrolyte volume to completely saturate both electrodes and the separator. The device was then encased in a Swagelok-type arrangement to maintain uniform pressure and avert electrolyte evaporation. This stringent assembly methodology guarantees that the documented internal resistance and cycling stability accurately represent the practical performance of the PrGO material.

CV analysis was performed to investigate the electrochemical properties of PrGO over an optimized voltage range. The following equation was used to compute the specific capacitance (C_s) from CV curves:

$$C_s = \frac{A}{2mKV} \quad (1)$$

Additionally, GCD tests were carried out at varied current densities across fixed voltage ranges to assess the charging–discharging performance and the cycling stability of the as-prepared materials and constructed supercapacitor cell. The C_s based on the GCD was calculated using eqn (2):

$$C_s = \frac{I\Delta t}{m\Delta V} \quad (2)$$

The two key factors that define the performance of the SCs are energy and power density. How much energy a gadget holds is referred to as energy density. The following formula was used to determine the energy density:

$$E = \frac{1}{2} \times C(\Delta V)^2 \Big/ 3.6 \quad (3)$$

How rapidly a device can discharge its energy is referred to as an SC's power density. The above formula was used to determine the power density (PD) of the constructed gadget.

$$\mathrm{PD} = \frac{E \times 3600}{\Delta t} \quad (4)$$

Device capacitivity and cycling stability are shown by the most likely rectangular CV curve. GCD measurements were taken at varied current densities in the potential window of 0 to 1 V. Charging and discharging processes cause galvanostatic charge/discharge curves to rise and then fall. Device impedance was measured using EIS data.

In the above equations, C_s, A, m, k, V, Δt, ΔV, C, and E represent the specific capacitance, absolute surface area covered by the CV curve, mass of the coated electrode material (in mg), scan rate (in mV s^{-1}), the voltage difference between the CV curves ($V_2 - V_1$), discharging period in seconds, potential window, specific capacitance at a certain current density and energy density of the device at a particular current density, respectively.

4. Results and discussion

4.1. Optimization of carbonization temperature and heating rate

The carbonization temperature and heating rate are critical parameters governing the yield, structural evolution, and graphitic ordering of biomass-derived carbon materials. Therefore, a systematic optimization was carried out to identify conditions that balance material yield with desirable structural characteristics for electrochemical applications.

TGA was first employed to examine the thermal decomposition behavior and carbon yield of the persimmon-derived hydrogel as a function of carbonization temperature (Fig. 1(a)). The results indicate a progressive decrease in the yield of the pyrolysis product with increasing final temperature, declining from 41.4% at 600 °C to 21.7% at 1000 °C. This trend is attributed to enhanced devolatilization, cleavage of oxygen-containing functional groups, and aromatization at elevated temperatures, which collectively promote mass loss. While lower temperatures preserve higher yields, insufficient carbonization limits structural ordering. Conversely, excessively high temperatures lead to pronounced material loss without proportionate improvements in graphitic structure. Based on this balance, 800 °C was identified as an optimal carbonization temperature, providing an acceptable yield (34.67%) while ensuring effective thermal reduction and carbon framework development.

The structural evolution of the carbon materials obtained at different temperatures was further evaluated using Raman spectroscopy (Fig. 1(b)). All pyrolyzed samples exhibited the characteristic D band (~1350 cm^{-1}) and G band (~1592 cm^{-1}), corresponding to defect-induced disorder and in-plane stretching of sp^2-hybridized carbon, respectively. With increasing carbonization temperature, a gradual enhancement in the intensity of the G band and improved definition of the Raman features were observed, indicating progressive structural ordering. However, the persistence of a prominent D band across all temperatures reflects the retention of defects and edge sites, which are typical of reduced graphene oxide–like materials derived from biomass precursors. Notably, the spectral evolution from 800 °C to higher temperatures showed only marginal improvements, suggesting that further thermal treatment does not significantly enhance graphitization.

Complementary insights into the long-range structural ordering were obtained from XRD analysis (Fig. 1(c)). The XRD patterns show a broad diffraction peak centered around $2\theta \approx 24°$, characteristic of the (002) plane of turbostratic or disordered graphitic carbon. Increasing the carbonization temperature resulted in a modest increase in peak intensity and slight narrowing up to 800 °C, indicative of improved stacking and partial graphitic ordering. Beyond this temperature, no substantial changes in the diffraction profiles were observed, confirming that higher thermal treatment does not yield significant structural benefits.

After establishing 800 °C as the optimal carbonization temperature, the influence of heating rate on carbon yield was investigated by TGA at ramp rates of 5, 10, and 15 °C min^{-1} (Fig. 1(d)). The lowest heating rate (5 °C min^{-1}) resulted in a substantially reduced yield (18.2%), which can be attributed to prolonged exposure to intermediate temperatures, leading to excessive decomposition and volatilization. In contrast, higher heating rates of 10 and 15 °C min^{-1} significantly improved the yield to 34.39% and 36.82%, respectively. As the difference in yield between these two rates was minimal, a heating rate of 10 °C min^{-1} was selected as an optimal condition, offering controlled carbonization while minimizing unnecessary mass loss.

Based on the combined TGA, Raman, and XRD analyses, the optimized synthesis conditions were established as carbonization at 800 °C with a heating rate of 10 °C min^{-1}, followed by a dwell time of 60 min and controlled cooling of 2 °C min^{-1}. The resulting material, denoted as PrGO, exhibits a reduced graphene oxide–like structure with favorable defect density and partial graphitic ordering, making it well suited for electrochemical energy storage applications. Although the carbonization temperature was optimized based on structural evaluation and material yield, the electrochemical performance of the optimized sample was subsequently investigated in acidic, neutral, and basic electrolytes, while a systematic comparison with other temperatures will be explored in future work.

4.2. Structural and chemical characterization of optimized PrGO

Following the optimization of the carbonization temperature and heating rate, the structural and chemical properties of the optimized PrGO, synthesized at 800 °C with a heating rate of 10 °C min^{-1}, were systematically investigated to elucidate its reduced graphene oxide–like nature and potassium incorporation.

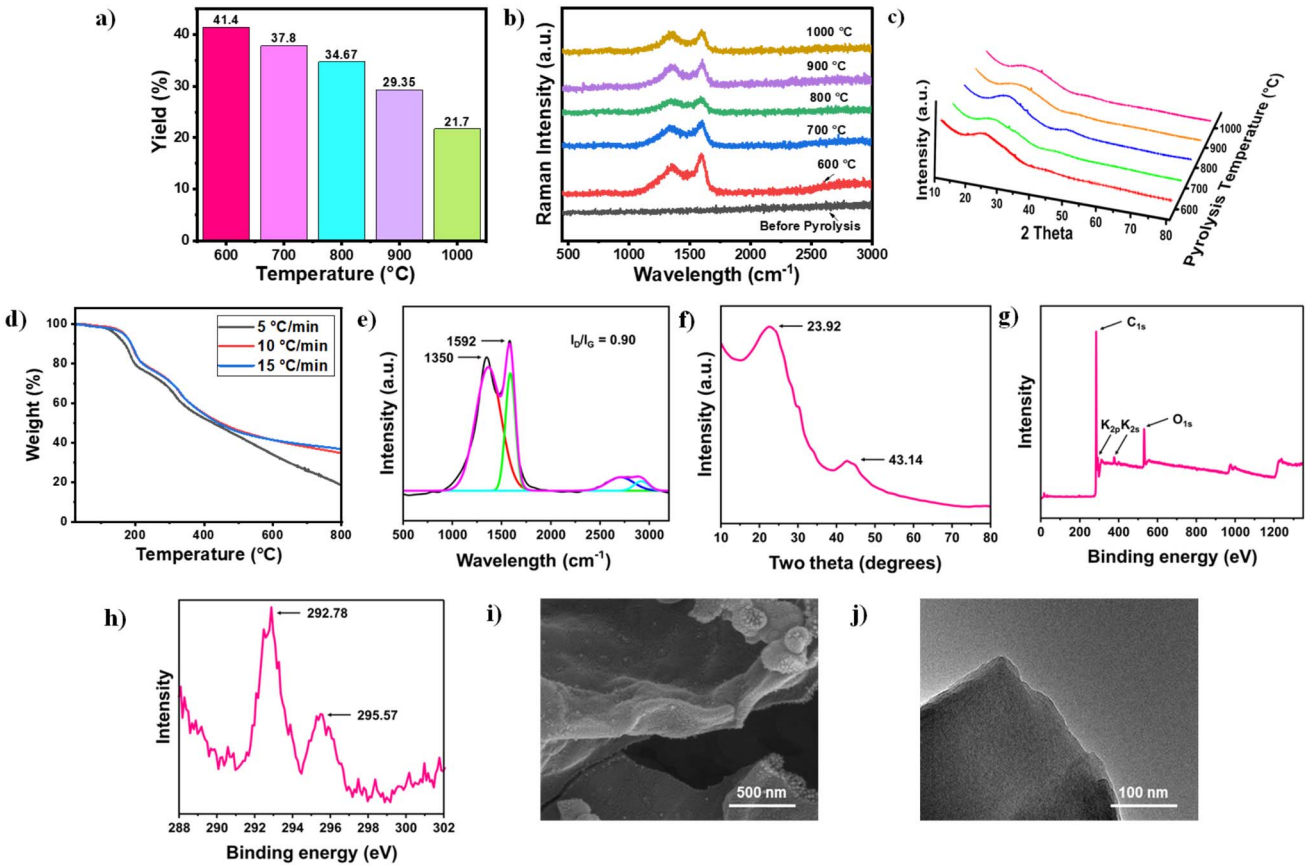

Fig. 1 (a) Residual yield as a function of pyrolysis temperature; (b) Raman spectra and (c) XRD patterns of samples pyrolysed at different temperatures (600–1000 °C); (d) TGA curves at different heating rates (5–15 °C min^{-1}). Data for PrGO synthesized under optimized conditions (800 °C and 10 °C min^{-1}): (e) Raman spectrum, (f) XRD pattern, (g) XPS survey spectrum, (h) high-resolution K 2p XPS spectrum, (i) SEM image (500 nm), and (j) HR-TEM image (100 nm).

Raman spectroscopy provided insights into the structural characteristics of graphene-based materials.[33,34] The data showed the presence of two characteristic bands, *i.e.* D & G bands, located at wavenumbers of 1350 cm^{-1} and 1592 cm^{-1}, respectively with an ID/IG ratio of 0.90 (Fig. 1(e)). The D band is associated with structural instability, while the G band is caused by the stretching of carbon sp^2 atoms.[35,36] Two additional bands are observed around 2700 and 2900 cm^{-1}, corresponding to the 2D band and the (D + G) combination mode, respectively. These two supplementary bands originated from the imperfections found in the graphitic arrangement of the carbon substance.

Raman spectroscopy was further analyzed to explicitly examine the characteristics of the 2D band. The Raman spectrum of PrGO shows a discernible 2D band centered at ~2708 cm^{-1}. Peak deconvolution (Gaussian fitting) reveals that the 2D band exhibits a large full width at half maximum (FWHM) of ~317 cm^{-1}, indicating significant structural disorder. The 2D band is broad and of low intensity relative to the G band, suggesting that the material does not consist of single-layer graphene. Instead, the pronounced broadening and reduced intensity of the 2D peak indicate the presence of few-layer graphene with turbostratic stacking and limited long-range order, which is characteristic of reduced graphene oxide–like (rGO-like) carbon materials.

Furthermore, the ID/IG ratio of 0.90 supports the presence of defect-rich graphene-like domains. This value falls within the optimal range (0.8–1.0) reported for biomass-derived graphene-like materials used in supercapacitor applications, where a balanced degree of disorder enhances electrochemical performance.[37]

This structural disorder can be attributed to the partial retention of oxygen-containing functional groups and defect formation during the pyrolysis of the persimmon-derived hydrogel. Such functional groups disrupt the continuity of the sp^2 carbon network by introducing vacancies, edge defects, and local lattice distortions, thereby enhancing the D-band intensity. Consequently, the Raman results indicate that the disordered structure of PrGO originates from defect sites associated with residual functional groups and imperfect graphitic domains formed during thermal conversion.

XRD was used to analyze the crystallinity or amorphous nature of the produced PrGO. After undergoing pyrolysis (thermal reduction), a broad peak becomes visible for PrGO at a 2θ value of 23.92° (Fig. 1(f)). This suggests that the pi-conjugated structure of graphene has been significantly

restored in PrGO and the (002) broad peak reflects a random crystal phase.[6,9] The material's random arrangement during the formation of a few layers of PrGO *via* pyrolysis, specifically a broad peak at $2\theta = 23.92°$ in XRD, strongly correlated with the D band observed in the Raman data. This correlation can be attributed to the disorderness of the PrGO.[38]

To determine the sample thickness and number of layers it contains, Scherrer's and Bragg's equations were used, as detailed in prior studies.[39–41] To determine the number of layers, divide the crystal size (C) by the interlayer distance (d) and then add one.[39–42] The crystal size (C) of the material has been calculated as 2.32 nm using the diffraction peak at $2\theta = 23.92°$. The interlayer spacing (d) of the PrGO material, determined from this peak, is 0.67 nm. This value is significantly larger than the typical interlayer distance of reduced graphene oxide (rGO), which generally ranges from ~0.34 to 0.39 nm. The increased interlayer distance in PrGO can be attributed to the swelling nature of the biomass precursor. During the initial hydrothermal treatment followed by freeze-drying, it is plausible that the precursor structure is retained, and subsequent thermal exfoliation in the second heating step (800 °C) further increases the spacing between graphene-like layers. The XRD results indicate the presence of a few layers—about 3–4 layers of graphene in PrGO. It was also discovered that the thin rGO nanosheets were stacked together, forming a thick, layered structure due to significant van der Waals interactions between layers.[43] Another less intense peak at $2\theta = 43.14°$ with (001) orientation was associated with the turbostratic band of disorganised carbon materials.[38]

The BET results of the samples before and after pyrolysis at 800 °C reveal a 69.8% increase in specific surface area, rising from 37.1 $m^2 g^{-1}$ to 63.0 $m^2 g^{-1}$ after pyrolysis (SI, Fig. S2). This indicates the development of a more accessible surface upon thermal treatment and additional porosity within the carbon framework.

Although the obtained surface area is moderate, this can be attributed to the restacking of graphene layers; however, it remains consistent with biomass-derived rGO materials.[44,45] For instance, oil palm waste-derived rGO has been reported to exhibit relatively low surface areas (as low as 8–15 $m^2 g^{-1}$) due to restacking and blocked pores, despite successful graphitization.[44] Similarly, the α-Fe_2O_3/ZnO/rGO heterostructure derived from basil seed (*Ocimum basilicum* L.) shows a moderate surface area of 24.569 $m^2 g^{-1}$.[45]

In addition, the total pore volume increases from 0.14 to 0.17 $cm^3 g^{-1}$, further confirming the formation of an expanded pore network. The average pore diameter decreases from 15.53 nm to 10.77 nm, indicating the development of a more refined mesoporous structure (SI, Fig. S2). A mesoporous architecture of PrGO is beneficial for supercapacitor applications, as it facilitates efficient ion diffusion and minimizes transport resistance. The increased surface area provides more active sites for charge accumulation, while the interconnected mesopores enhance electrolyte accessibility and ion mobility.

The full scan XPS measurements of PrGO indicate the presence of carbon, oxygen, and potassium with atomic percentages of 88.41, 9.05, and 2.15, respectively. Fig. 1(g) shows the XPS full-scan, with C 1s, O 1s, K $2p_{3/2}$, K $2p_{1/2}$, and K 2s peaks located at 284.50 eV, 531.78 eV, 292.08 eV, 295.57 eV and 378.9 eV.[21] Fig. 1(h) shows two different peak satellites corresponding to K $2p_{3/2}$ and K $2p_{1/2}$ at 292.93 eV and 295.70 eV, respectively.[46] Four peaks from the deconvolution of C 1s spectra have been positioned at 284.50 eV, 286.10 eV, 292.71 eV, and 295.74 eV. The strength of the peaks at 284.50 eV is higher, indicating that PrGO is mostly associated with sp^2 hybridization (C=C) and confirming the presence of a pi network in the synthesised PrGO. The peak at 286.10 eV is attributed to C–O functional groups, while the higher binding energy features at 292.71 and 295.74 eV are assigned to π–π* shake-up satellite transitions associated with aromatic sp^2 carbon domains (SI, Fig. S3). The binding energy values for O 1s revealed that oxygen exists in two distinct chemical environments, with C=O at 530.86 eV and C–O at 532.30 eV (SI, Fig. S4).

The FTIR spectrum of PrGO exhibits key vibrational features indicative of potassium-coordinated oxygen functionalities. A broad band centred at 1566 cm^{-1} corresponds to the asymmetric stretching vibration of the carboxylate group, while a weaker band at 1378 cm^{-1} is assigned to the symmetric COO^- stretching. A very small and broad peak in the 1700–1730 cm^{-1} region suggests that most carboxylic acid groups have been deprotonated, confirming the formation of potassium carboxylate (COO–K^+) species. Additionally, a broad and intense peak around 1200 cm^{-1} is attributed to overlapping contributions from C–O–C asymmetric stretching and C–O vibrations of residual oxygen-containing groups, potentially stabilized by potassium coordination (SI, Fig. S5). TGA analysis was performed to study the thermal stability of the material. TGA data show a two-stage thermal decomposition. In the first stage (up to 380 °C) a lower weight loss was observed due to the removal of absorbed water molecules or physically attached functional groups while the second stage weight loss (temperature higher than 380 °C) was due to decomposition of the material (SI, Fig. S6).

4.3. Surface properties

SEM analysis was performed to examine the surface morphology of the PrGO. As shown in Fig. 1(i), at a magnification of 500 nm, the material exhibits a distinct sheet-like structure. To further analyze the surface features, a 3D surface plot and roughness measurements were generated using ImageJ software ((SI, Fig. S7(a–d)). Fig. S7(a) was used to generate a hill stack view of the surface, shown in Fig. S6(b), which shows the uneven arrangement of graphene sheets with varying sheet areas, curling edges, and sharp spikes. The presence of these morphological defects results in a higher defect concentration, enhancing the metallic properties of the nanosheets and contributing to their excellent conductivity.

The 3D surface plot of the selected area of Fig. S7(c), shown in Fig. S7(d), further highlights the corrugated edges and the interconnected stacking of graphene sheets, held together by van der Waals forces. Such surface roughness and structural irregularities are expected to increase ion accessibility and thus significantly enhance the material's capacitive performance.

The SEM observations are consistent with the FT-IR, Raman, and XRD results, all of which confirm the formation of few-layered PrGO sheets. Finally, a supercapacitor was fabricated using PrGO as the electrode material to validate its promising capacitive behaviour.

The internal morphology of the PrGO was obtained by HR-TEM analysis. A high resolution TEM image shows the sheet-like structure of the PrGO (Fig. 1(j)). Fig. S8(a–c) revealed the presence of 3–4 layers in PrGO, which also resembled the XRD findings. The hill stack plot diagram based on HR-TEM at 50 nm magnification (Fig. S7(d)) reveals the rough surface of the nanosheets, which have ridged edges that make them well-suited for supercapacitor applications. The data on surface roughness aligns well with the SEM results. In addition, Fig. S8(e) presents a 3D surface plot of the highlighted region of the HR-TEM image, generated using the Fire LUT in ImageJ. In this plot, darker blue regions correspond to lower height values, typically only a few nanometers, while lighter regions represent higher surface features. A colour scale bar has also been added to provide a quantitative reference for these height variations, further highlighting the grain boundaries and layered structure within the sample.

5. Electrochemical performance of the PrGO

5.1. Cyclic voltammetry (CV)

The electrochemical study of PrGO was initially evaluated using a 3-electrode system with 1 M H_2SO_4 as the electrolyte. The CV curves with the potential range of −0.1 to 1.1 V are shown in Fig. 2(a). Different scan rates of 2, 5, 10, 20, 50, 100, and 200 mV s^{-1} were used to determine the C_s of PrGO. The results of these measurements were about 302, 284, 260, 209, 146, 109, and 60 F g^{-1}, respectively (Table 1).

It was noticed that the CV curves retained a quasi-rectangular shape over the entire range of scan rates, indicating dominant electric double-layer capacitance (EDLC) behavior. Although the specific capacitance decreased with increasing scan rate due to diffusion limitations of electrolyte ions at higher rates, the overall shape preservation confirms good rate capability and efficient charge-storage kinetics.

5.2. Galvanostatic charge/discharge (GCD)

The supercapacitive behaviour of the produced electrode was extensively investigated through GCD tests. These tests were conducted at current densities ranging from 0.5 to 10 A g^{-1}, within a potential window of −0.1 to 1.1 V. Fig. 2(b) shows the GCD profiles for PrGO at different current densities, while keeping the potential constant at 1.2 V. The material exhibited a higher C_s of 412 F g^{-1} at a current density of 0.5 A g^{-1}. Although the current density was raised, the C_s experienced a slight decrease to 215 F g^{-1} at 10 A g^{-1} (Table 2). The material demonstrated excellent capacitance and impressive rate capacity in terms of its GCD behavior. The low resistance of ion transport and the short diffusion distance during the charging-discharging process contribute to this phenomenon.

5.3. Electrochemical impedance spectroscopy (EIS)

EIS analysis was performed to assess the internal resistance/impedance of the material, as well as to examine the diffusion kinetics and transportation behavior of electrolyte ions. This analysis utilized a 1 M H_2SO_4 electrolyte and covered a frequency range of 10 mHz to 10^6 Hz. The Nyquist plot, shown in Fig. 2(c), depicts the relationship between the real impedance (Z) and the imaginary impedance (Z'') of various devices. It is worth noting that the plot exhibits a rising trend in the low-frequency range, which suggests the capacitive characteristics of the synthesized material. In general, the Nyquist plot consists of a semicircle along with a straight line at a 90-degree angle. This semicircle symbolizes the charge-transfer-resistance (R_{ct}) that exists between the electrode and electrolyte. Fig. 2(d) clearly illustrates a small semi-circular region in the plot, which suggests that there may be low faradaic resistances in the electrolyte. The intersection point of the X-axis in the EIS plot, known as the Nyquist plot, is referred to as the equivalent series resistance (ESR). The ESR encompasses several factors, including the resistance of materials, the resistance of electrolytic ions, and the resistance at the contact point between the current collector and the electrode material. The material exhibited a significantly low internal resistance of $R_{eq} = 0.96\ \Omega$ in the higher frequency range, indicating its great conductivity and superior electrochemical performance.

To further understand the influence of the electrolyte environment, the electrochemical performance of PrGO was additionally investigated in neutral (2 M KCl) and alkaline (6 M KOH) electrolytes. The corresponding CV, GCD, and EIS profiles are provided in SI, Fig. S9 and S10, while the calculated specific capacitance values are summarized in Tables 1 and 2. Compared to the acidic medium, a gradual decrease in capacitance is observed in neutral and alkaline electrolytes, which can be attributed to the lower ionic conductivity, larger hydrated ionic radius, and slower diffusion kinetics of K^+ ions. These results confirm the strong dependence of electrochemical performance on electrolyte properties.

5.4. Electrochemical performance of the device

Additionally, in order to assess its feasibility in real-time supercapacitors, we constructed a symmetric SC device using an aqueous 1 M H_2SO_4 electrolyte and studied its performance using CV, GCD, and EIS techniques. Fig. 3(a) shows the CV curves obtained from the fabricated device using the synthesized material. The measurements were conducted at various scan rates ranging from 2 to 200 mV s^{-1} within a potential range of 0 to 0.9 V. All of the CV curves displayed leaf-like shapes that were similar. The C_s of the fabricated device was calculated at different scan rates of 2 to 200 mV s^{-1} and the obtained values of C_s are listed in Table 3. Furthermore, the device underwent GCD experiments, where current densities ranged from 0.2 A g^{-1} to 3 A g^{-1}. Fig. 3(b) shows the device-specific capacitances at different current densities. The calculated capacitance for different current densities is given in Table 4.

One notable advantage of supercapacitors is their long-term cycling stability. In order to ensure the stability of a SC device

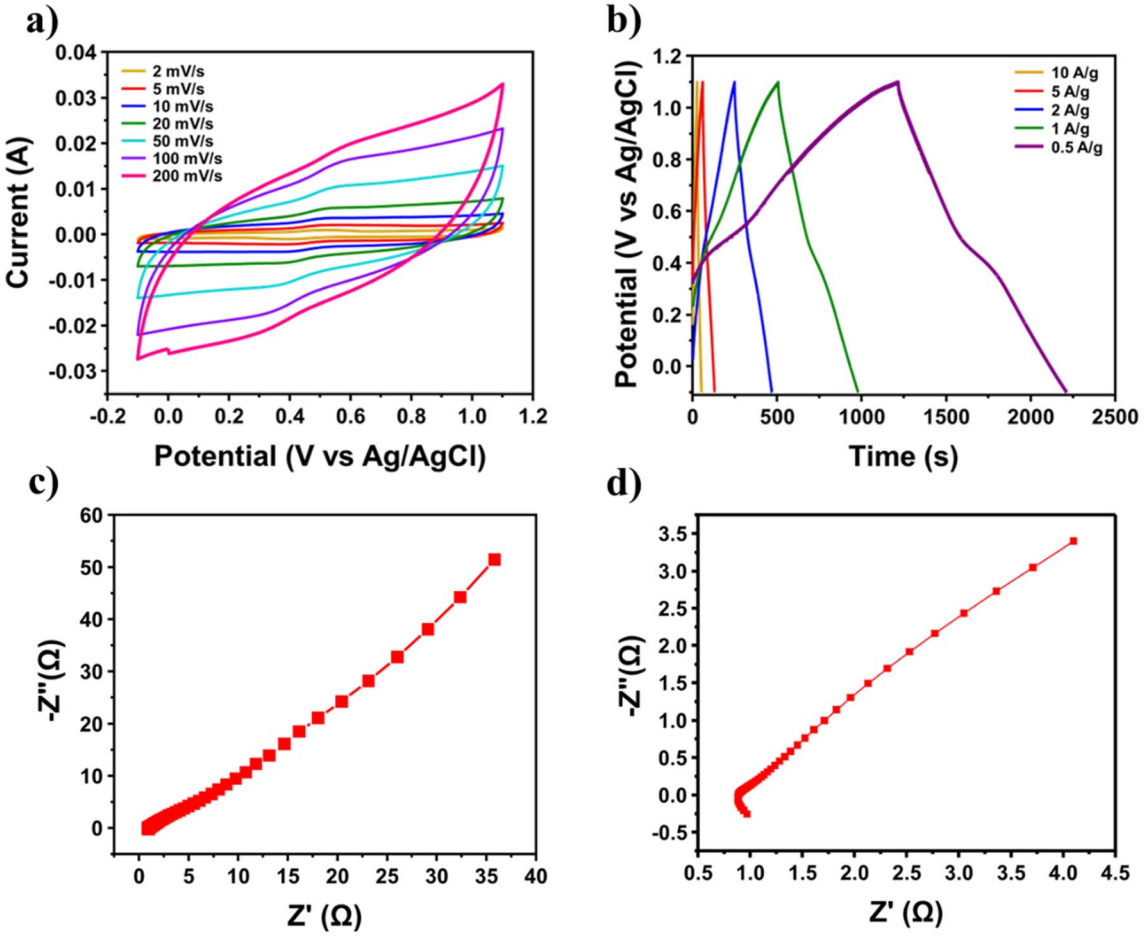

Fig. 2 (a) CV plots at numerous scan rates, (b) GCD at different current densities, (c) Nyquist plot, and (d) magnified view of the Nyquist plot.

Table 1 The specific capacitance of PrGO at different scan rates

Scan rate (mV s^{-1})		2	5	10	20	50	100	200
Specific capacitance (F g^{-1})	1 M H_2SO_4	302.08	284.16	260.10	209.58	146.54	109.29	60.79
	2 M KCl	293.12	223.14	178.32	135.61	80.05	54.10	36.45
	6 M KOH	152.55	100.23	69.12	51.15	35.35	26.42	19.42

over a large number of cycles, it is essential to conduct a cycling stability test. Fig. 3(c) illustrates the cycling stability of the device in terms of C_s and percentage capacitance retention. The device was tested within a potential window of 0 to 0.9 V at a high current density of 50 A g^{-1} for 5000 cycles in a 1 M H_2SO_4 solution. Based on the information provided in Fig. 3(d), it is evident that the device exhibits a capacitance retention of 78% after undergoing 5000 cycles. Although traditional EDLCs generally demonstrate over 90% capacitance retention, the approximately 78% retention reported in our K-doped rGO-like material can be ascribed to several causes. The first is the substantial contribution to pseudocapacitance brought about by potassium doping and residual oxygen functional groups. Nevertheless, compared to pure electrostatic charge storage,

Table 2 The specific capacitance of PrGO at different current densities

Current density (A g^{-1})		0.5	1	2	5	10
Specific capacitance (F g^{-1})	1 M H_2SO_4	412.70	396.33	369.70	298.00	215.00
	2 M KCl	192.42	143.12	94.22	67.31	—
	6 M KOH	46.12	34.02	22.54	15.33	—

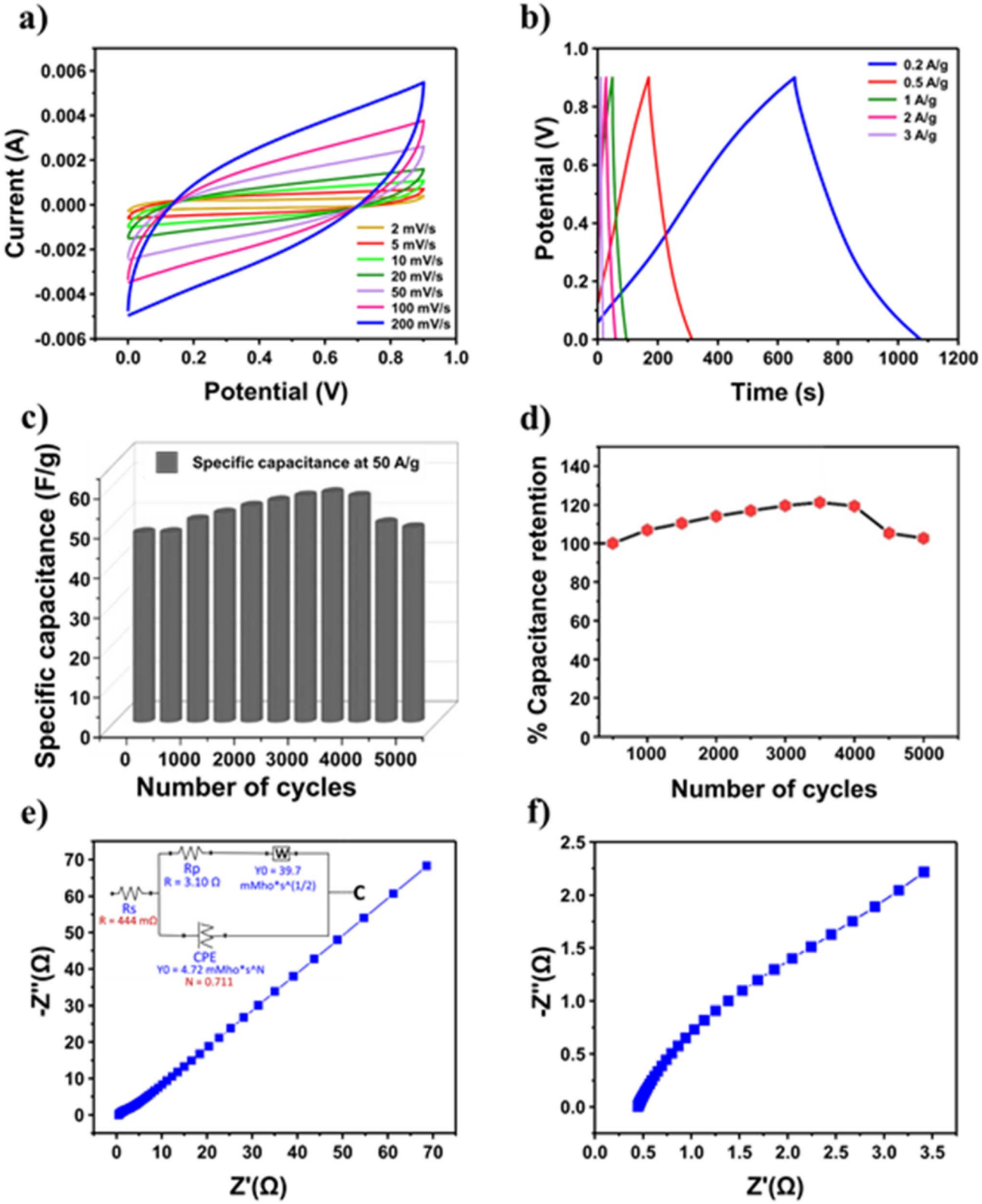

Fig. 3 (a) CV plots at numerous scan rates, (b) GCD plots at numerous current densities, (c) cycling stability, (d) % capacitance retention of the fabricated SC device, (e) Nyquist plot of the PrGO derived SC device (inset: equivalent circuit model used for fitting), and (f) magnified view of the Nyquist plot.

Table 3 The specific capacitance of PrGO at different scan rates

Scan rate (mV s^{-1})	2	5	10	20	50	100	200
Specific capacitance (F g^{-1})	161.02	130.42	93.10	64.22	40.34	28.76	21.00

Table 4 The specific capacitance of PrGO at different current densities

Current density (A g^{-1})	0.2	0.5	1	2	3
Specific capacitance (F g^{-1})	98.00	82.20	72.00	59.05	43.20

these faradaic processes are intrinsically less stable, and capacitance fading occurs as a result of the irreversible redox consumption of surface functional groups during cycling.[47] The second point is that with an acidic electrolyte (H_2SO_4), the active K-sites and large surface area can cause the electrolyte to decompose locally at the electrode interface or even evolve into gas (H_2/O_2 evolution). This would lead to micropore blockage and an increase in internal resistance during prolonged cycling.[48] Thirdly, the effective accessible surface area decreases over continuous cycling due to partial pore blockage or ion entrapment, especially within micropores, in the hierarchical porous structure.[49] The apparent trade-off between high capacitance and moderate cycling stability is accounted for by these combined effects.

The study utilized EIS to identify the equivalent sheet resistance (ESR) or cell internal resistance. The frequency range used for the study was 10 mHz to 10^6 Hz. Based on the data from Fig. 3(e and f), we observed that the fabricated device exhibited a lower ESR value, approximately 0.65 ohms. The low equivalent series resistance (ESR) can be attributed to potassium-induced electronic modulation, where K acts as an n-type dopant, enhancing the electrical conductivity of the rGO framework. In addition, the expanded interlayer spacing and defect-rich structure improve electrolyte wettability and ion transport, thereby facilitating charge transfer kinetics and decrease resistance at the electrode/electrolyte contact.[50,51] The synthesized material exhibits excellent supercapacitive performance as an electrode material for supercapacitors, as evidenced by its low ESR value. Furthermore, the device exhibits an energy density of approximately 11.0 Wh kg^{-1}, accompanied by a power density of 89.8 W kg^{-1}, when operating at a low current density of 0.2 A g^{-1}. The comparison of capacitance, power density (ES), and ESR values of PrGO with other graphene-based materials is given in the SI (Tables S2 and S3).

6. Computational analysis of PrGO

Density functional theory (DFT) based computational investigations have been performed to understand the structural, electronic and capacitive aspects of the PrGO. The computational PrGO material has been designed using the XPS data to closely mimic its experimental counterpart as shown in Table 5. Initially, the theory has been evaluated for the pristine graphene, and thereafter utilized for the PrGO. The density functional simulations utilize Generalized Gradient Approximation (GGA) with Perdew–Burke–Ernzerhof (PBE) parameterization, along with Grimme-D2 van der Waals correction.[52] The high symmetry points of the Brillouin zone in the reciprocal space have been sampled with *k*-points of 30*30*1 and 7*7*1 for a primitive cell of pristine graphene having 2 atoms and a supercell of PrGO having 54 atoms, respectively. Sufficiently large *k*-points of 27*27*1 have been utilized to accurately extract the density of states (DOS). The structural relaxations are performed using the limited memory Broyden–Fletcher–Goldfarb–Shanno (L-BFGS) algorithm to achieve the defined force and stress tolerances of 0.05 eV $Å^{-1}$ and 0.1 GPa, respectively.

The relaxed atomic structures of simulated pristine graphene and PrGO are shown in Fig. 4. Computationally, all the properties of pristine graphene can be extracted by simulating its primitive cell consisting of 2 atoms. The lattice constant and carbon–carbon bond length of pristine graphene are 2.465 Å and 1.42 Å, respectively.

The computed electronic band structure and DOS profiles (Fig. 4(b)) of pristine graphene show a perfect Dirac cone shape (at the *k*-point of the Brillouin zone in band structure). The investigation of partial DOS reveals that the states near the Fermi level arise only from the *p*-states of carbon, which can be attributed to the aromaticity or delocalization of the π–cloud from the p_z-orbitals. While designing the PrGO nanosheet (Fig. 4(c)), a double vacancy (DV) defect has been created in the 5*5 supercell of graphene to position four carbonyl (R═O) groups. A hydroxyl (R–OH) group is also inserted into the supercell to achieve the targeted oxygen concentration. It has been noted that all the carbon atoms associated with the carbonyl and hydroxyl groups have slightly shifted out of plane, indicating their hybridization transformation from sp^2 to sp^3. Our previous study indicated that substitutional doping of potassium is more favorable in graphene,[53] and thus potassium is originally inserted at a single vacancy (SV) site through substitutional doping prior to structural relaxation. However,

Table 5 The atomic composition of the PrGO

Element	XPS data	Computational design
Carbon	88.41	87.03
Oxygen	9.05	9.25
Potassium	2.15	1.85
Miscellaneous	0.39 (Unknown)	1.85 (Hydrogen)

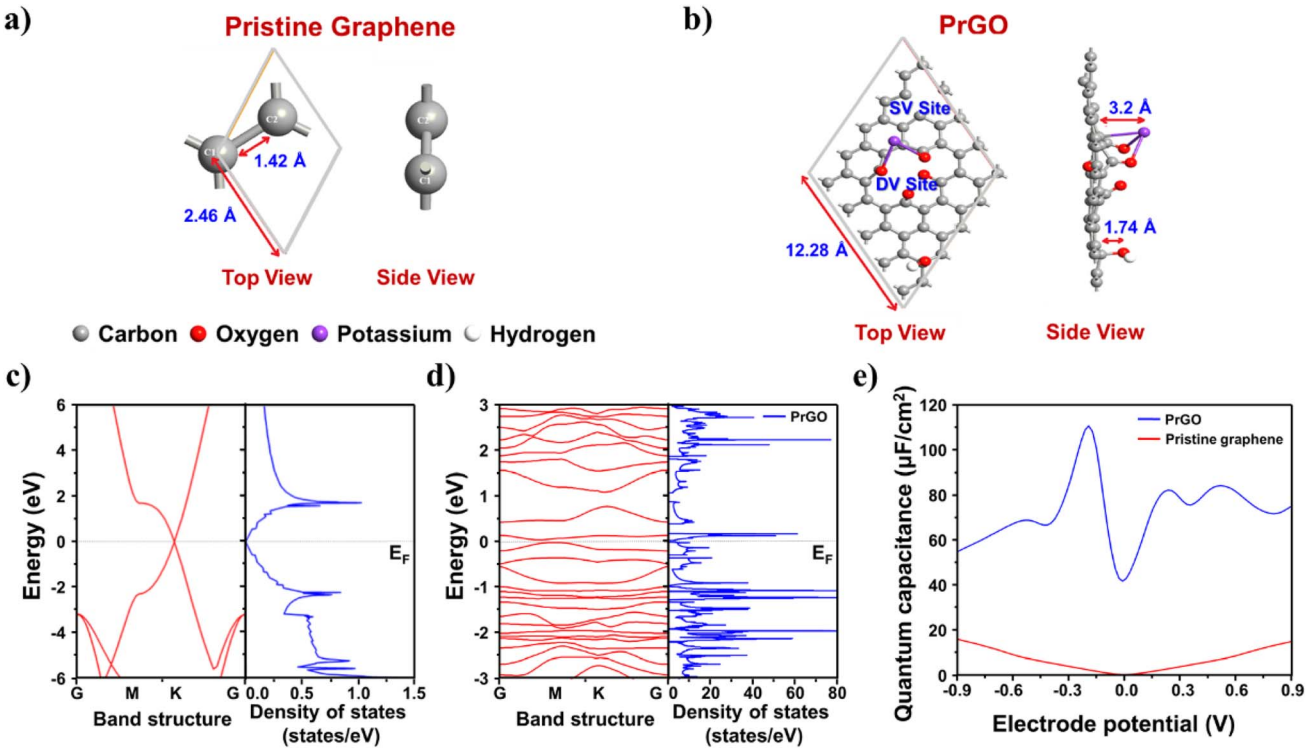

Fig. 4 The relaxed atomic structures of simulated (a) pristine graphene and (b) PrGO. The electronic band structure and density of states (DOS) profiles of (c) pristine graphene, (d) PrGO (here, the Fermi level is shifted to energy zero), and (e) quantum capacitance offered by pristine graphene and PrGO.

post structural relaxation, the potassium atom is observed to vacate its most favorable SV site in graphene and bond with the oxygen atoms of rGO. This can be attributed to the very high electronegativity of oxygen (3.44 by the Pauling scale) in comparison to potassium (0.82 by the Pauling scale). Thus, potassium is most likely bonded with the oxygens in the synthesized PrGO. The electronic band structure and DOS profile of PrGO are shown in Fig. 4(d), where a large number of states are observed near the Fermi level in contrast to pristine graphene, which can be attributed to the presence of defects and non-carbon elements. These large number of states have a significant influence on the quantum capacitance offered by the PrGO.

The quantum capacitance offered by pristine graphene and PrGO has been extracted to understand their behavior as supercapacitor electrodes. Quantum capacitance is inherent to the nano-materials due to the electronic compressibility and the low DOS.

The DOS (D(E)) dependent quantum capacitance (C_Q) is extracted using the MATLAB programing[54] of the following expressions,[55,56]

$$C_Q = \frac{1}{V_e}\int_0^V C_Q^{diff}(V)\mathrm{d}V \quad (5)$$

where

$$C_Q^{diff} = \frac{e^2}{4KT}\int_{-\infty}^{\infty} D(E)\sec h^2\left(\frac{E+V}{2KT}\right)\mathrm{d}E$$

Here, V is the applied electrode voltage, e is elementary charge, E is energy, K is Boltzmann's constant, and T is temperature.

The computational quantum capacitance extracted for pristine graphene and PrGO as supercapacitor electrodes is depicted in Fig. 4(e), where the values for pristine graphene are in good agreement with those experimentally reported by Ponomarenko *et al.*[57] The pristine graphene offers negligible quantum capacitance at zero potential, which increases gradually as the potential is varied, owing to its Dirac cone structure of DOS near the Fermi level. The maximum quantum capacitance offered by the pristine graphene within the considered electrochemical range is 16.52 μF cm^{-2} at −0.9 V. On the other hand, the PrGO offers substantially higher quantum capacitance than the pristine graphene, portraying its suitability as a supercapacitor electrode. The peak quantum capacitance offered by PrGO is 110.75 μF cm^{-2} at −0.19 V, which is about 6.7 times higher than that of pristine graphene. Moreover, the PrGO offers significant quantum capacitance on both the positive and negative sides of the electrochemical window, indicating its suitability for symmetric supercapacitors.

7. Conclusion

In this study, few-layer reduced graphene oxide (rGO) was successfully synthesized from persimmon fruit using a clean, two-step thermal method. A systematic optimization of carbonization temperature and heating rate enabled the identification of suitable conditions for obtaining a conductive,

graphene-like structure. The formation and quality of the rGO-like material (PrGO) were confirmed through comprehensive characterization techniques including Raman spectroscopy, XRD, FTIR, XPS, SEM, HR-TEM, and TGA. XPS analysis revealed a natural potassium doping level of 2.15 atomic percent, contributing to the material's enhanced electrochemical properties. The electrochemical performance of the synthesized material, *i.e.*, PrGO, was investigated in three different electrolytes, *i.e.* 1 M H_2SO_4 (acidic), 2 M KCl (neutral) and 6 M KOH (alkaline), using a three-electrode setup. The maximum C_s achieved was 302 F g^{-1} at a scan rate of 2 mV s^{-1} in the acidic electrolyte. Additionally, a symmetric supercapacitor (SC) device fabricated using PrGO achieved a high specific capacitance of 98 F g^{-1}, an energy density of 11 Wh kg^{-1}, and a power density of 89.8 W kg^{-1} at a current density of 0.2 A g^{-1}. The device also demonstrated excellent cycling stability, retaining 78% of its initial capacitance after 5000 charge–discharge cycles. DFT calculations were performed to support the experimental results and assess the quantum capacitance behavior of PrGO. While pristine graphene showed low quantum capacitance near zero potential, PrGO exhibited a significantly higher value of 110.75 μF cm^{-2} at −0.19 V—approximately 6.7 times greater than that of pristine graphene. Moreover, PrGO maintained appreciable quantum capacitance across both positive and negative potentials, highlighting its promise for symmetric supercapacitor configurations. Overall, this work demonstrates the feasibility of producing potassium-doped, few-layer rGO from persimmon fruit as a low-cost electrode material. The combined experimental and computational insights underline its strong potential for high-performance supercapacitors and future applications in energy storage technologies.

Author contributions

Chetna Tewari-conceptualization, methodology, experimentation, investigation, and drafting the original manuscript, Kundan Singh Rawat-writing and reviewing the manuscript, Diksha Bhatt-electrochemical analysis and contributed to the writing, Boddepalli SanthiBhushan and Anurag Srivastava-computational analysis and writing, Young Nam Kim and Somi Yoon-characterization. Nanda Gopal Sahoo-electrochemical analysis and review and editing of the manuscript, Jun-Wei Zha-investigation, Yong Chae Jung-conceptual guidance, supervision, review and editing.

Conflicts of interest

The authors declare that they have no known competing financial interests or personal relationships that could have appeared to influence the work reported in this paper.

Data availability

The datasets generated during and/or analysed during the current study will be made available by the corresponding author on reasonable request. All other supporting data are included within the article and its supplementary information (SI). Supplementary information: additional characterization data (XPS, FTIR, BET, TGA, SEM, and TEM images with 3D surface plots), as well as supplementary figures and tables supporting the conclusions of this study. See DOI: https://doi.org/10.1039/d6ta01141a.

Acknowledgements

The authors acknowledge the National Research Council of Science and Technology (NST) grant from the Korean government (MSIT) (CRC23013-000) and the KIST Institutional Program for provided funding for this work.

References

1 Y. Shang, Y. Huang, L. Li, F. Wu and R. Chen, *Chem. Rev.*, 2025, **125**, 5674–5744, DOI: 10.1021/acs.chemrev.4c00863.
2 K. S. Rawat, C. Tewari, T. Arya, Y. N. Kim, P. Pant, S. Sati, S. Dhali, P. B. Negi, Y. C. Jung and N. G. Sahoo, *Next Energy*, 2025, **6**, 100209, DOI: 10.1016/j.nxener.2024.100209.
3 N. Choudhary, A. Tomar, S. Bhardwaj, J. Ćwiertnia, D. Just, D. Janas, R. Chandra and P. K. Maji, *J. Mater. Chem. A*, 2025, **13**, 4012–4042, DOI: 10.1016/j.rser.2025.116624.
4 M. Murugan, G. Dineshkumar, K. C. Kumar, C. Tewari, M. Ganesan, N. G. Sahoo and M. Sivanantham, *J. Electrochem. Soc.*, 2023, **170**, 040518, DOI: 10.1149/1945-7111/acbf7b.
5 C. Tewari, Y. N. Kim, H. Muramatsu, M. Endo, Y. A. Kim and Y. C. Jung, *Langmuir*, 2023, **39**, 6698–6704, DOI: 10.1021/acs.langmuir.3c00092.
6 K. S. Rawat, C. Tewari, T. Arya, P. Pant, Y. N. Kim, R. Kumar, Y. C. Jung, N. G. Sahoo and J. Power, *Sour*, 2026, **661**, 238601, DOI: 10.1016/j.jpowsour.2025.238601.
7 P. Ponmani, J. Bahadur, C. Tewari, D. K. Gupta, U. Kalita, P. Jegadeesan, T. R. Ravindran, A. Alex, A. Das, N. G. Sahoo and M. Sivanantham, *J. Polym. Sci.*, 2023, **61**, 2149–2162, DOI: 10.1002/pol.20220709.
8 C. Tewari, K. S. Rawat, Y. N. Kim, T. Arya, S. Dhali, S. Rana, D. V. Andreeva, B. Özyilmaz, R. Mahfouz, N. Qari, Y. C. Jung, N. G. Sahoo and K. S. Novoselov, *Renew. Sustain. Energy Rev.*, 2026, **226**, 116443, DOI: 10.1016/j.rser.2025.116443.
9 J. Masa and W. Schuhmann, *Chem. Cat. Chem.*, 2019, **11**, 5842–5854, DOI: 10.1002/cctc.201901151.
10 A. Morenghi, S. Scaravonati, G. Magnani, M. Sidoli, L. Aversa, R. Verucchi, G. Bertoni, M. Riccò and D. Pontiroli, *Electrochim. Acta*, 2022, **424**, 140626, DOI: 10.1016/j.electacta.2022.140626.
11 T. Khandaker, T. Islam, A. Nandi, M. A. A. M. Anik, M. S. Hossain, M. K. Hasan and M. S. Hossain, *Sustain. Energy Fuels*, 2025, **9**, 693–723, DOI: 10.1039/D4SE01393J.
12 K. Radhakrishnan and A. Kumar, *Renew. Sustain. Energy Rev.*, 2026, **229**, 116624, DOI: 10.1016/j.rser.2025.116624.
13 M. Cao, Y. Hu, W. Cheng, S. Huan, T. Bai, Z. Niu, Y. Zhao, G. Yue, Y. Zhao and G. Han, *Chem. Eng. J.*, 2022, **436**, 135233, DOI: 10.1016/j.cej.2022.135233.

14 D. C. Wang, H. Y. Yu, Z. Ouyang, D. Qi, Y. Zhou, A. Ju, Z. Li and Y. Cao, *Nanoscale*, 2022, **14**, 5163–5173, DOI: 10.1039/D2NR00030J.
15 O. Akhavan, K. Bijanzad and A. Mirsepah, *RSC Adv.*, 2014, **4**, 20441–20448, DOI: 10.1039/C4RA01550A.
16 G. Tatrari, C. Tewari, M. Pathak, M. Karakoti, B. S. Bohra, S. Pandey, B. SanthiBhushan, A. Srivastava, A. Rana and N. G. Sahoo, *J. Energy Storage*, 2022, **53**, 105098, DOI: 10.1016/j.est.2022.105098.
17 I. Berktas, M. Hezarkhani, L. Haghighi Poudeh and B. Saner Okan, *Graphene Technol.*, 2020, **5**, 59–73, DOI: 10.1007/s41127-020-00033-1.
18 Y. Shen, *Renew. Sustain. Energy Rev.*, 2026, **225**, 116206, DOI: 10.1016/j.rser.2025.116206.
19 S. Kumar, C. Tewari, N. G. Sahoo and L. Philip, *J. Hazard. Mater.*, 2022, **435**, 128956, DOI: 10.1016/j.jhazmat.2022.128956.
20 L. E. Chaney, J. Hui, H. You, Y. Zhou, J. R. Downing, W. Y. Chen, E. Benson, J. B. Dunn, S. J. Rowan and M. C. Hersam, *npj Adv. Manuf.*, 2026, **3**, 3, DOI: 10.1038/s44334-025-00063-8.
21 X. Su, L. Ge, S. Huang, X. Wang, H. Xie, Y. Liu, L. Yi, L. Liu, J. Meng and H. Meng, *Biomass Bioenergy*, 2026, **208**, 108876, DOI: 10.1039/D5NA00705D.
22 C. Tewari, Y. Kim, Y. N. Kim, S. Ryu, H. S. Jeong and Y. C. Jung, *J. Vinyl Addit. Technol.*, 2023, **30**, 102–113, DOI: 10.1002/vnl.22032.
23 H. R. Barai, N. S. Lopa, P. Barai, M. M. Rahman, A. K. Sarker and S. W. Joo, *J. Mater. Sci.: Mater. Electron.*, 2019, **30**, 21269–21277, DOI: 10.1007/s10854-019-02500-9.
24 M. Liu, J. Niu, Z. Zhang, M. Dou and F. Wang, *Nano Energy*, 2018, **51**, 366–372, DOI: 10.1016/j.nanoen.2018.06.037.
25 Q. Li, X. Ye, Y. Jiang, E. H. Ang, W. Liu, Y. Feng, X. Rui and Y. Yu, *Mater. Chem. Front.*, 2021, **5**, 3132–3138, DOI: 10.1039/D0QM00990C.
26 F. Nathania and T. Nurkhoeriyati, Drying technologies utilized to preserve persimmon fruits (Diospyros kaki L.): A review. in *IOP Conference Series: Earth and Environmental Science*. IOP Publishing, 2025, 1445, 1, p. 012004.
27 A. Celik and S. Ercisli, *Int. J. Food Sci. Nutr.*, 2008, **59**, 500–606, DOI: 10.1080/09637480701538221.
28 J. Tao, A. Mu, S. Geng, H. Xiao, L. Zhang and Q. Huang, *J. Solid State Electrochem.*, 2021, **25**, 1959–1974, DOI: 10.1007/s10008-021-04984-0.
29 X. Liu, Y. Tong, Y. Wu, J. Zheng, Y. Sun, L. Niu and H. Li, *Chem. Eng. J.*, 2022, **431**, 133986, DOI: 10.1016/j.cej.2021.133986.
30 A. Testoni, First Mediterranean symposium on persimmon, *Cah. Options Mediterr*, 2022, **51**, 53–70. https://om.ciheam.org/article.php?IDPDF=2600062.
31 C. G. Park, K. C. Lee, D. W. Lee, H. Y. Choo and P. J. Albert, *J. Chem. Eco.*, 2024, **30**, 2269–2283, DOI: 10.1023/B:JOEC.0000048788.35693.23.
32 M. S. Butt, M. T. Sultan, M. Aziz, A. Naz, W. Ahmed, N. Kumar and M. Imran, *EXCLI Journal*, 2015, **14**, 542–561, DOI: 10.17179/excli2015-159.
33 P. Pérez-Martínez, J. M. Galvan-Miyoshi and J. Ortiz-López, *J. Mater. Sci.*, 2016, **51**, 10782–10792, DOI: 10.1007/s10853-016-0290-0.
34 L. Stobinski, B. Lesiak and A. Malolepszy, *J. Electron Spectrosc. Relat. Phenom.*, 2014, **195**, 145–154, DOI: 10.1016/j.elspec.2014.07.003.
35 A. C. Ferrari, *Solid State Commun.*, 2007, **143**, 47–57, DOI: 10.1016/j.ssc.2007.03.052.
36 S. Jaworski, M. Wierzbicki, E. Sawosz, A. Jung, G. Gielerak, J. Biernat, H. Jaremek, W. Łojkowski, B. Woźniak, J. Wojnarowicz and L. Stobiński, *Nanoscale Res. Lett.*, 2018, **13**, 1–17, DOI: 10.1186/s11671-018-2533-2.
37 M. Athanasiou, S. N. Yannopoulos and T. Ioannides, *Chem., Eng., J.*, 2022, **446**, 137191, DOI: 10.1016/j.cej.2022.137191.
38 N. M. S. Hidayah, W. W. Liu, C. W. Lai, N. Z. Noriman, C. S. Khe, U. Hashim and H. C. Lee, *Comparison on graphite, graphene oxide and reduced graphene oxide: Synthesis and characterization*, AIP Publishing, 2017, p. 1892, DOI: 10.1063/1.5005764.
39 G. Pavoski, T. Maraschin, F. Fim, N. Balzaretti, G. Galland, C. Moura and N. Basso, *Mater. Res.*, 2017, **20**, DOI: 10.1590/1980-5373-MR-2015-0528.
40 S. K. Sahoo and A. Mallik, *Nano*, 2015, **10**, 1550019, DOI: 10.1142/S1793292015500198.
41 J. Aladekomo and R. Bragg, *Carbon*, 1990, **28**, 897–906, DOI: 10.1016/0008-6223(90)90338-Y.
42 E. Aliyari, M. Alvand and F. Shemirani, *RSC Adv.*, 2016, **6**, 64193–64202, DOI: 10.1039/C6RA04163A.
43 D. Li, M. B. Muller, S. Gilje, R. B. Kaner and G. G. Wallace, *Nat. Nano.*, 2008, **3**, 101–105, DOI: 10.1038/nnano.2007.451.
44 S. Nasir, M. Z. Hussein, N. A. Yusof and Z. Zainal, *Nanomaterials*, 2017, **7**, 182, DOI: 10.3390/nano7070182.
45 A. Sanei, K. Dashtian, J. Y. Seyf, F. Seidi and E. Kolvari, *J. Environ. Management*, 2023, **332**, 117377, DOI: 10.1016/j.jenvman.2023.117377.
46 X.-R. Li, J. Liu, F.-Y. Kong, X.-C. Liu, J.-J. Xu and H.-Y. Chen, *Electrochem. Commun.*, 2012, **20**, 109–112, DOI: 10.1016/j.elecom.2012.04.014.
47 M. Sevilla and R. Mokaya, *Energy Environ. Sci.*, 2014, **7**(4), 1250–1280.
48 G. Wang, L. Zhang and J. Zhang, *Chem. Soc. Rev.*, 2012, **41**(2), 797–828.
49 E. Huarote-Garcia, A. A. Cardenas-Riojas, I. E. Monje, E. O. López, O. M. Arias-Pinedo, G. A. Planes and A. M. Baena-Moncada, *ACS Environ. Au*, 2024, **4**(2), 80–88.
50 E. Zhou, J. Xi, Y. Liu, Z. Xu, Y. Guo, L. Peng, W. Gao, J. Ying, Z. Chen and C. Gao, *Nanoscale*, 2017, **9**(47), 18613–18618.
51 N. Sumathi, A. C. Dhanemozhi, D. Thangaraju, S. A. Adewinbi, K. Mohanraj, R. Marnadu and M. Shkir, *Surf. Interfaces*, 2021, **26**, 101408.
52 QuantumATK, *Synopsys QuantumWise A/S*, accessed on Jan. 15, 2024. [Online]. Available: https://www.synopsys.com/silicon/quantumatk.html.
53 C. Tewari, B. SanthiBhushan, A. Srivastava and N. G. Sahoo, *Sustain. Chem. Pharm.*, 2021, **21**, 100436, DOI: 10.1016/j.scp.2021.100436.

54 MATLAB, The MathWorks Inc., accessed on Jan 15, 2024. [Online]. Available: https://www.mathworks.com.
55 A. Srivastava and B. SanthiBhushan, *Appl Nanosci.*, 2018, **8**, 637–644, DOI: 10.1007/s13204-018-0643-x.
56 B. SanthiBhushan, and A. Srivastava, in *AIP Conference Proceedings*, 1953, no. 1. AIP Publishing, 2018. DOI: 10.1063/1.5033300.
57 L. A. Ponomarenko, R. Yang, R. V. Gorbachev, P. Blake, A. S. Mayorov, K. S. Novoselov, M. I. Katsnelson and A. K. Geim, *Phys. Rev. Lett.*, 2010, **105**, 136801, DOI: 10.1103/PhysRevLett.105.136801.